Two-Dimensional Lateral Epitaxy of 2H (MoSe₂)−1T′ (ReSe₂) Phases

Amey Apte,[†] Aravind Krishnamoorthy,[‡] Jordan A. Hachtel,[§] Sandhya Susarla,[†] Jongwon Yoon,[∥] Lucas M. Sassi,[†] Palash Bharadwaj,[⊥] James M. Tour,[†,∥] Juan Carlos Idrobo,[§] Rajiv K. Kalia,[‡] Aiichiro Nakano,[‡] Priya Vashishta,*,[‡] Chandra Sekhar Tiwary,*,[†,#] and Pulickel M. Ajayan*,[†]

[†]Department of Materials Science and NanoEngineering, Rice University, 6100 Main Street, Houston, Texas 77005, United States

[‡]Collaboratory for Advanced Computing and Simulations, Department of Physics and Astronomy, Department of Computer Science, Department of Chemical Engineering and Materials Science, Department of Biological Sciences, University of Southern California, Los Angeles, California 90007, United States

[§]Center for Nanophase Materials Sciences, Oak Ridge National Laboratory, Oak Ridge, Tennessee 37831, United States
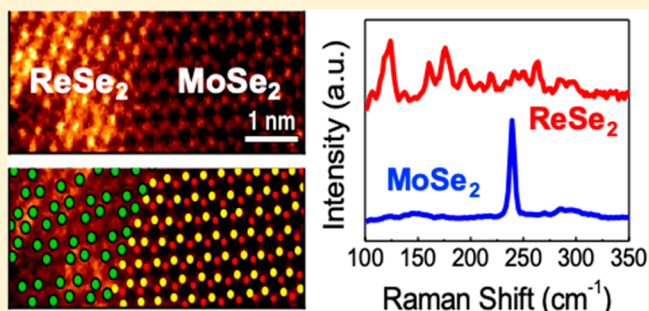
[∥]Department of Chemistry, Rice University, 6100 Main Street, Houston Texas 77005, United States

[⊥]Department of Electrical and Computer Engineering, Rice University, 6100 Main Street, Houston, Texas 77005, United States

S Supporting Information

ABSTRACT: Two-dimensional (2D) transition metal dichalcogenide (TMDC) heterostructures have been proposed as potential candidates for a variety of applications like quantum computing, neuromorphic computing, solar cells, and flexible field effective transistors. The 2D TMDC heterostructures at the present stage face difficulties being implemented in these applications because of lack of large and sharp heterostructure interfaces. Herein, we address this problem via a CVD technique to grow thermodynamically stable heterostructure of 2H/1T′ MoSe₂−ReSe₂ using conventional transition metal phase diagrams as a reference. We demonstrate how the thermodynamics of mixing in the MoReSe₂ system during CVD growth dictates the formation of atomically sharp interfaces between MoSe₂ and ReSe₂, which can be confirmed by high-resolution scanning transmission electron microscopy imaging, revealing zigzag selenium-terminated interface between the epitaxial 2H and 1T′ lattices. Our work provides useful insights for understanding the stability of 2D heterostructures and interfaces between chemically, structurally, and electronically different phases.

KEYWORDS: Two-dimensional materials, heterostructures, transition metal dichalcogenides

Two-dimensional materials such as graphene, boron nitride, transition metal dichalcogenides (TMDCs)/oxides (TMOs), and so forth have exhibited interesting properties compared to their bulk counterparts.[1−9] Heterostructures of van der Waals' solids, which are composite materials made up of stacked atomically thin two-dimensional materials are also broadly studied. The idea, widely reviewed by Geim et al., envisages a sequence of stacking individual two-dimensional materials on top of each other to realize certain increased chemical stability and emergent properties for applications.[10] A number of top-down and bottom-up techniques such as mechanical exfoliation, single/multistep vapor deposition, and wet chemical synthesis have been demonstrated for producing a variety of promising functional heterostructures such as graphene/TMDCs, TMDC/TMDC, metal/TMDC, and so forth. A few notable examples of such heterostructures includes MoS₂, WS₂, h-BN, or In₂Se₃ on graphene for novel photodetectors, MoS₂/WS₂ heterobilayers for two-dimensional field effect transistors, and Pt or Ag/MoS₂ for electro-catalysis of hydrogen evolution reaction

(HER).[11−17] Creating heterostructures by mechanical exfoliation results in extremely sharp and clean interfaces, but the coverage area is small and the method is only limited to nonepitaxial vertical stacking.[18] On the other hand, wet chemical synthesis results in large scale production of heterostructures with little control over quality.[19] Single and multistep chemical vapor deposition (CVD) has been reported to give the most reliable results.[20−23] As a result, a number of CVD techniques for growing MX₂ heterostructures (M = Mo/W, X = S/Se) have been reported and studied for their interesting band alignments, possibility of generating interlayer excitons, and strong coupling, ultrafast charge transfer, and strain engineering.[23−29] However, the lateral and vertical heterostructure formation between the ubiquitous MoX₂/WX₂ system is considered to be a kinetic process, and hence successful synthesis using CVD method depends on a lot of
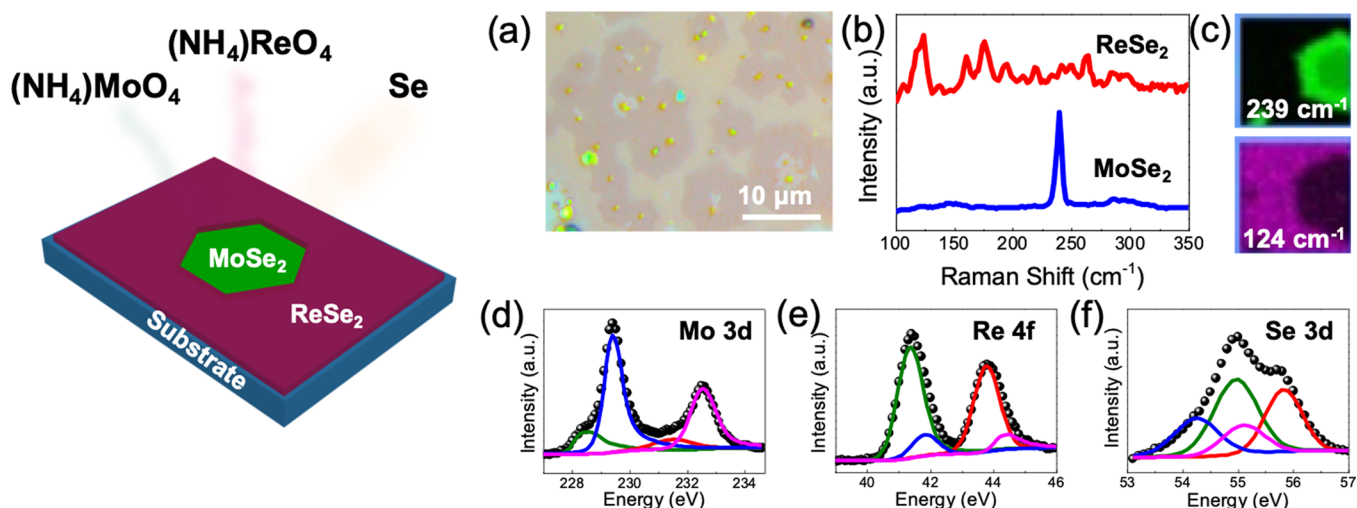
Figure 1. Synthesis and characterization of the $ReSe_2-MoSe_2$ heterostructures. (a) Optical image showing the monolayer $MoSe_2$ hexagonal flakes (dark) in monolayer $ReSe_2$ matrix (light). (b) Raman spectra of the two regions shows distinct signals corresponding to the $MoSe_2$ and $ReSe_2$ structures, which is confirmed by (c) spatial mapping; the green map shows the signal of 239 cm^{-1} mode of $MoSe_2$ (top) whereas the magenta map shows the 124 cm^{-1} mode of $ReSe_2$, confirming the heterojunction (d−f) High-resolution XPS spectra showing presence of Mo 3d, Re 4f, and Se 3d signals in the synthesized samples.

experimental variables such gas flow, position of precursors, time of evaporation of precursors, and so forth which makes it tricky to reproduce.

Adopting a thermodynamic approach for synthesizing heterostructures would be more beneficial as the process would be more controlled and easily reproducible and would result in a sharp interface. Using $ReSe_2/MoSe_2$ as a model system, we have designed a route to thermodynamically stable lateral TMDC heterostructures using the corresponding transition metal binary phase diagrams as a reference. Rhenium diselenide ($ReSe_2$) is a group VII transition metal dichalcogenide material which stabilizes in the distorted 1T (i.e., 1T′) phase due to the presence of extra electron in the d-orbital of rhenium which hybridizes with the p-orbital of the chalcogen giving rise to octahedral coordination.[30,31] There is Peierls distortion in $ReSe_2$ which lowers the overall symmetry of this structure but causes the individual layers to be decoupled from each other even in bulk state, something that does not occur in Mo and W-based TMDCs.[31] Combination of $ReSe_2$ with $MoSe_2$ makes it a nonisomorphous system. Recently, we reported controlled doping of Re atoms in monolayer $MoSe_2$ lattice via chemical vapor deposition; steadily incorporating a greater amount of Re destabilizes the 2H phase of $MoSe_2$ and instead results in the 1T′ structure ($Re_{1-x}Mo_xSe_2$).[32] Such phase transformed alloys also exhibited emergent magnetism despite not being composed of conventional magnetic elements.

In this work, we report the synthesis and characterization of lateral heterostructure between monolayer $MoSe_2$ and $ReSe_2$ with 2H and 1T′ symmetries respectively (referred to as "RMS heterostructures"). The heterostructure was grown via chemical vapor deposition technique and characterized by a host of methods; the individual domains of single crystalline $MoSe_2$ are easily identifiable in a matrix of $ReSe_2$ via optical microscope and exhibit atomically sharp α-type zigzag heterojunctions in high-angle annular dark-field scanning transmission electron microscopy (HAADF-STEM). Raman spectroscopy showed characteristic peaks for $MoSe_2$ and $ReSe_2$ lattices arising from their distinct symmetries. The Raman

maps further clarified the existence of a lateral heterostructure. X-ray photoelectron spectroscopy was used to identify the Re and Mo states and binding energies showing minimal doping. Density functional theory (DFT) simulations showed that the stable α interface representing the lowest energy configuration is nonmagnetic and laterally delineates the monolayer 2H $MoSe_2$ and 1T′ $ReSe_2$ domains with minimal cationic substitutions. Further, the formation of such a heterostructure results in dramatic reduction in bandgap with the valence and conduction band edge electronic states arising predominantly out of contribution from the molybdenum and rhenium atoms close to the atomically sharp interfaces. With the help of Mo−Re binary phase diagram, the reason for stability and large-scale formation of this novel two-dimensional 2H-1T′ heterostructure is explained.

The RMS heterostructures were grown via chemical vapor deposition (CVD) on single crystal sapphire (0001) substrates. The Mo and Re precursors were chosen as ammonium molybdate ((NH_4)$_2MoO_4$ Sigma-Aldrich, 99.99%) and ammonium perrhenate (NH_4ReO_4, Sigma-Aldrich, >99%) respectively. The relative ratio of the precursors was chosen as 2:1 by weight and they were placed in porcelain boats inside a 2 in. diameter quartz tube so as to reach temperatures of 600 and 500 °C. Selenium powder (100 mesh, 99.99%) was chosen as the chalcogen source in a similar porcelain boat placed upstream in a temperature zone of ∼250 °C. The sapphire substrates were placed in a separate boat downstream of the precursor boats. The tube furnace was ramped up to 600 °C in 20 min and held at that value for another 20 min before cooling down. High purity Ar/H_2 (15%) was used as the carrier gas for the growth. The heterostructures were obtained on the top surface of the sapphire substrates and transferred onto SiO_2/Si substrates via standard "PMMA+KOH" etching for better visual identification.

Raman and PL spectra were obtained on an inVia spectrometer by Renishaw with 532 nm laser and 10 s acquisition times. XPS spectra were collected on a PHI Quantera system using 1486.6 eV incident X-ray energy and 26 eV pass energy. STEM experiments were performed on a Nion
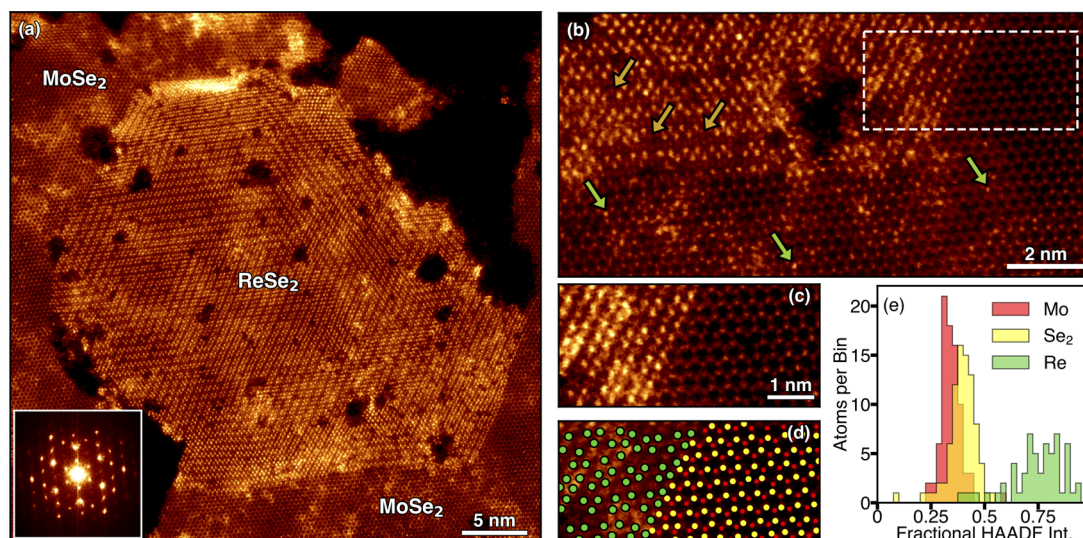
Figure 2. Atomic-resolution images of 1T′-ReSe$_2$ and 2H-MoSe$_2$ lateral heterostructures. (a) High-angle annular dark-field (HAADF) scanning transmission electron microscopy (STEM) image of a monolayer heterostructures between 1T′-ReSe$_2$ and 2H-MoSe$_2$. Inset: fast Fourier transform of image in (a) showing epitaxial crystallinity between the two phases. (b) Higher-resolution image of interface between ReSe$_2$ and MoSe$_2$. Some Mo atoms can be observed in 1T′-ReSe$_2$ lattice (orange arrows), and some Re atoms can be observed in 2H-MoSe$_2$ lattice (green arrows). Aside from a small degree of alloying, the interface is atomically sharp. (c) Highlighted region from (b). (d) Atomic-site positions for all atoms in 2H phase and anions in 1T′ phase. (e) Fractional HAADF intensities at the atomic positions in (d). It can be seen from relative HAADF intensities that red atoms are Mo, yellow atoms are Se, and green atoms are Re, indicating that the zigzag type interface is Se terminated.

aberration corrected UltraSTEM 100 operated at an accelerating voltage of 60 kV. The experiments were performed with a convergence semiangle of 30 mrad.

DFT simulations of lateral interfaces were performed on systems containing 216 atoms, corresponding to 36 formula units each of MoSe$_2$ and ReSe$_2$, in a simulation cell measuring 40.2 Å × 19.7 Å along the *a*- and *b*-directions. DFT simulations of pure MoSe$_2$ and ReSe$_2$ and alloyed Mo$_{1−x}$Re$_x$Se$_2$ crystals for calculation of free energies were performed on supercells comprising 6 × 6 × 1 unit cells containing 108 atoms. A vacuum of 15 Å is added along the *c*-axis of all simulation cells to remove spurious image interactions. Calculations were performed until each self-consistency cycle is converged in energy to within 1×10^{-5} eV/atom and forces on ions are under 1×10^{-2} eV/Å. Further details are given in Supporting Information.

Figure 1 shows the schematic of the heterostructures and the synthesis setup. The molybdenum and rhenium precursors were kept in individual porcelain boats at different positions as described in Methods. The heterostructure samples were obtained on the top surface of the sapphire substrate. However, to aid visual identification, the monolayers were transferred to a clean SiO$_2$/Si substrate (300 nm oxide layer) via standard PMMA-mediated procedures reported in the literature. Figure 1a shows a 50× magnification optical image of the transferred sample. Two distinct spatial domains can be clearly identified—the darker (roughly) hexagonal islands are MoSe$_2$ whereas the lighter matrix surrounding them is ReSe$_2$. The MoSe$_2$ islands are approximately 10 μm large and have small multilayers at their centers. Figure 1b shows the Raman spectra collected from the ReSe$_2$ (red) and MoSe$_2$ (blue) regions respectively; the MoSe$_2$ spectrum can be identified easily owing to the strong out-of-plane A$_{1g}$ mode at ∼239 cm^{-1}. The ReSe$_2$ spectrum is rich with at least 18 A$_g$ Raman active vibrational modes (e.g., 124, 161, 176 cm^{-1}, etc.) due to

the low symmetry of the $P\bar{1}$ space group and the distorted 1T phase.[33]

This picture is made even clearer once we look at the Raman intensity maps in Figure 1c. The upper map at 239 cm^{-1} (green) shows only the hexagonal MoSe$_2$ crystal with a black background, whereas the lower map at 124 cm^{-1} (magenta) shows the ReSe$_2$ region. Photoluminescence spectra of MoSe$_2$ (shown in Figure S1 in Supporting Information) reveal a relatively weak and somewhat broad resonance at 1.56 eV which corresponds to the monolayer optical band gap. This quenching of photoluminescence in the MoSe$_2$ region of the heterostructure is due to the donor-doping by Re atoms, which are thermodynamically predicted to be present in trace amounts in the MoSe$_2$ matrix and can be observed in atomic-resolution HAADF-STEM images (Figure 2). Previous studies have also demonstrated that small amounts of doping by donor atoms can lead to the formation of in-gap defect states leading to the reduction of the band gap.[34] The atomic force microscopy (AFM) analysis in Figures S2 and S3 confirms the planar nature of the heterostructure, as shown in the Supporting Information.

In order to understand the chemical composition of the heterostructure, the sample was studied with X-ray photoelectron spectroscopy. XPS is highly surface sensitive and can reveal information on the chemical bonding of the constituent atoms from the minor shifts in binding energies (BE) of their core electrons. Figure 1d−f shows the high-resolution XPS spectra of the Mo 3d, Re 4f, and Se 3d states, respectively. The Mo 3d spectrum in Figure 1d can be fit with two sets of 3d$_{5/2}$ (lower BE) and 3d$_{3/2}$ (higher BE) spin−orbit split peaks with a separation of 3.1 eV. The dominant 3d$_{5/2}$ peak at 229.4 eV is due to Mo atoms predominantly in the 2H phase of MoSe$_2$ as reported. The other 3d$_{5/2}$ peak occurring at a downshifted value of 228.6 eV could be due to Mo atoms in proximity to Re atoms either doped (lightly) in the MoSe$_2$ lattice or at the domain boundaries between the hexagonal islands and the
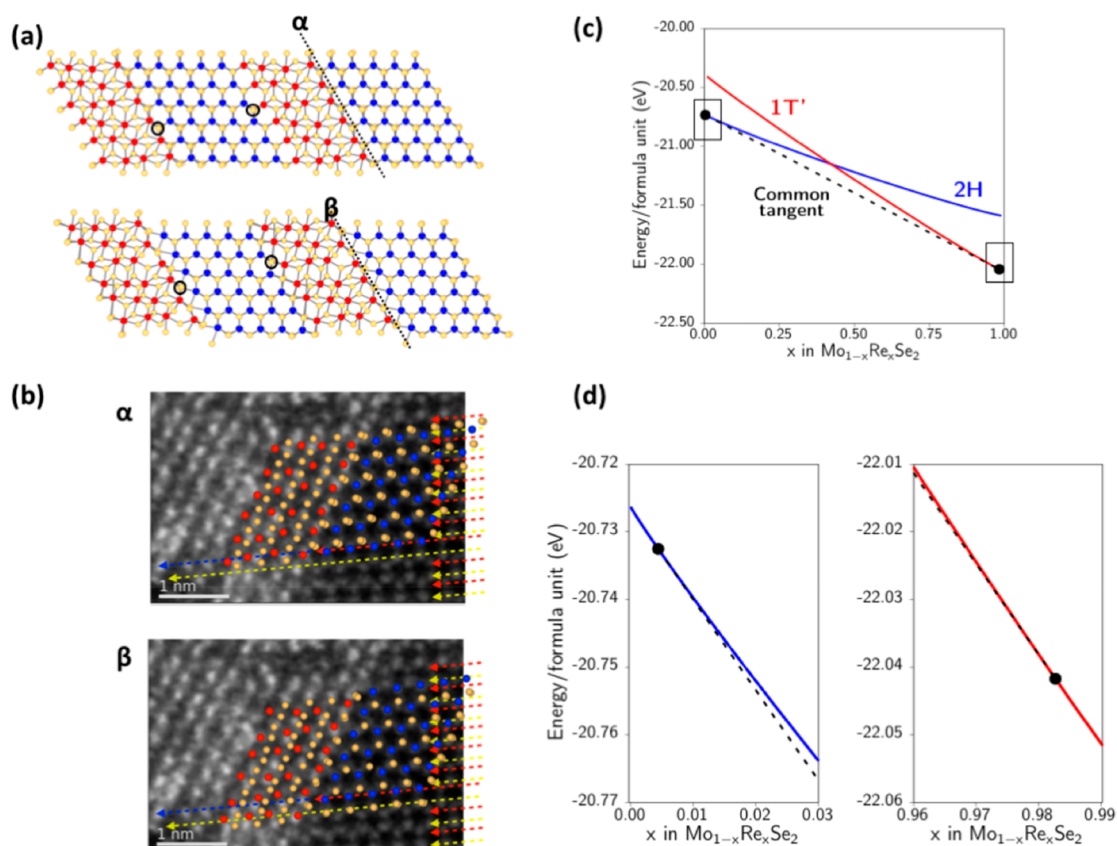
Figure 3. Structure and energetics of H-T′ interfaces. (a) Atomic structure of the α- (top) and β- (bottom) interfaces between $MoSe_2$ and $ReSe_2$ monolayers. Representative 3-fold- and 4-fold-corordinated Se ions at the α- and β-interfaces are highlighted by circles. (b) High-resolution scanning tunneling electron microscopy image of the $MoSe_2/ReSe_2$ interface overlaid with the computed atomic structure of the α- and β-interfaces shows better agreement between the observed experimental atomic positions and theoretical predictions in the α-interfacial structure. (c) Common tangent construction between free energy curves of $Mo_{1-x}Re_xSe_2$ alloys in the H and T′ crystal structures. Black dots denote the points of intersection of the common tangent between curves. (d) Zoomed-in views of highlighted areas near the common tangent intersections in (c) show that heterostructure formation occurs between 0.4% Redoped $MoSe_2$ and 1.3% Mo-doped $ReSe_2$.

surrounding matrix. Because Re atoms have an extra electron, their presence next to Mo atoms causes increasing shielding of the nuclear charge of the latter which in turn decreases the binding energy of the Mo 3d electrons. The corresponding $3d_{3/2}$ peaks appear at 232.5 and 231.7 eV. This is complemented by the Re 4f spectra in Figure 1e. The fitting yields a dominant $4f_{7/2}$ peak at 41.4 eV and weaker one at 41.9 eV, which can be assigned to the 1T′ phase of $ReSe_2$ (from the matrix) and for Re atoms at the heterojunction interfaces (and/or some light doping within the $MoSe_2$ lattices). The corresponding $4f_{5/2}$ pair of peaks appear with a separation of 2.45 at 43.8 and 44.3 eV. Finally, we see that the Se 3d spectra in Figure 1f shows an envelope that can be fitted with two pairs of peaks each with a mutual separation of 0.86 eV. These are attributed to the Se atoms bonding with Mo and Re atoms, respectively.

To better understand the interface between the different phases of the heterostructures the monolayer samples are examined with a scanning transmission electron microscope (STEM). The HAADF image in Figure 2a is a 2048 × 2048 pixel image with a 15 μs pixel dwell time over a 32 nm field-of-view (FOV). The HAADF images in Figure 2b,c are 1024 × 1024 pixel images with a 15 μs pixel dwell time over a 16 nm FOV. In both images, a Gaussian blur with $σ = 1$ is used to improve the signal-to-noise ratio. Figure 2a shows an atomic-resolution HAADF image of a monolayer 1T′-$ReSe_2$ region

surrounded by monolayer 2H-$MoSe_2$. We focus on an island of $ReSe_2$ surrounded by $MoSe_2$ to demonstrate the stability of the heterostructures but larger uniform grains of both materials are observed throughout the sample. The center region shows the coordinated 4-anion unit-cell pattern of the 1T′-$ReSe_2$ phase, while outer regions show the hexagonal structure of the 2H phase. Additionally, the difference between the $ReSe_2$ and $MoSe_2$ can also be observed by the apparent brightness of the center region of Figure 2a; because HAADF images are formed through Z-contrast, the heavy Re atoms ($Z = 75$) are much brighter than the Mo ($Z = 42$) and Se_2 ($Z_{eff} = 48.1$) columns. Furthermore, it can be seen that the two phases are epitaxial to one another by taking the fast Fourier transform (FFT) of the image (shown in the inset). Here, the FFT spots all show the same hexagonal symmetry; if the $ReSe_2$ phase had any rotation with respect to the surrounding $MoSe_2$, a separate spot would be visible in the FFT. It can also be seen that the crystallographic orientation of the 2H phases on either side of the 1T′ island are identical, further confirming the strong epitaxy of the heterostructure (Figure S4).

A higher-resolution HAADF image of the interface between the 1T′ and 2H regions is shown in Figure 2b. In the 2H-$MoSe_2$ region, there are many individual atoms that are much brighter than the other columns in the 2H lattice (a few have been highlighted with green arrows in Figure 2b), indicating that Re atoms have diffused out into the 2H region. Likewise, it
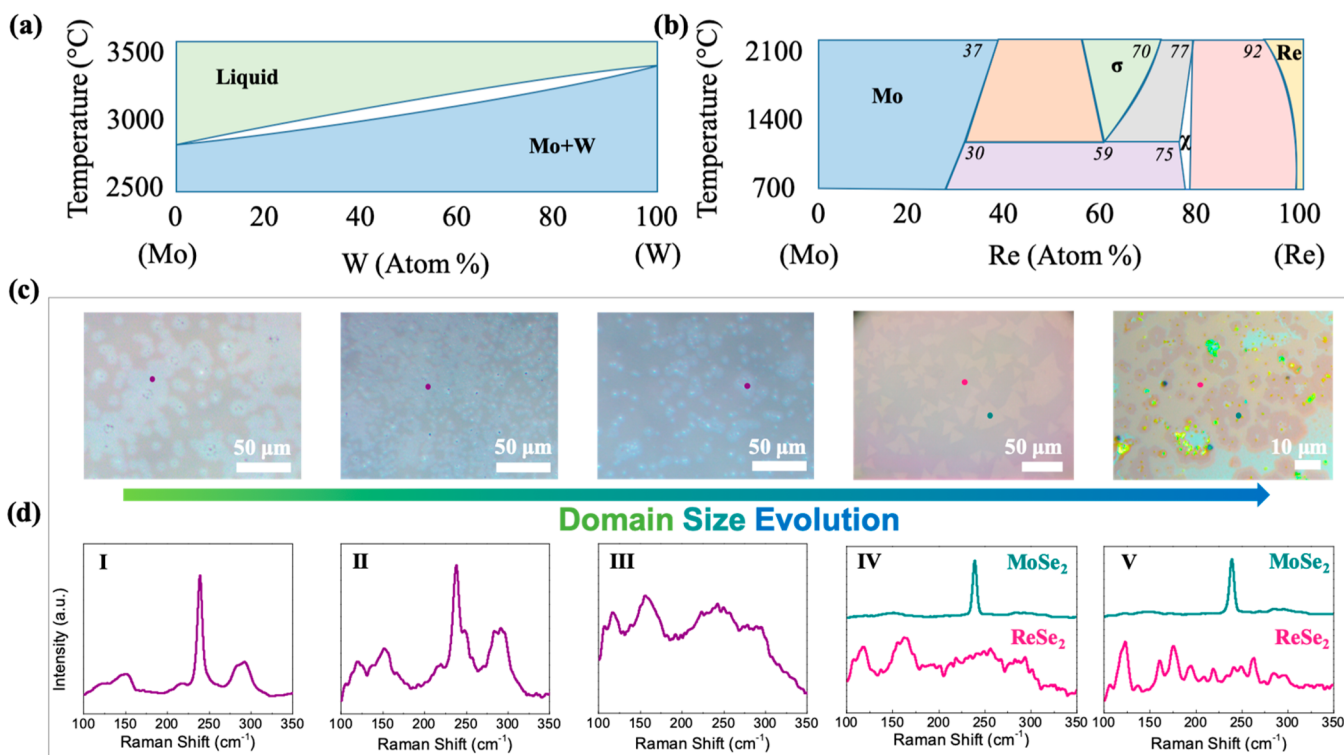
Figure 4. Domain size evolution in the 2D molybdenum rhenium selenide system. (a) Binary Mo−W phase diagram (b) binary Mo−Re phase diagram. The two diagrams illustrate the differences in miscibility of molybdenum with tungsten and rhenium, respectively. (c) Optical microscope images of CVD-synthesized 2D $Re_{1-x}Mo_xSe_2$ samples with five mixed compositions (Re ∼ 8%, 20%, and 40%) and two segregated compositions (Re > 40%). (d) Raman spectra of the five samples from the spots indicated in row (c) confirming gradual changes in composition pointing toward possible evolution of domain size and understood via phase diagram in (b). (Diagrams in (a,b) reproduced with permission from Springer Nature: S.V. Nagender-Naidu et al. Bulletin of alloy phase diagrams Vol. 5, Issue 2, pp.177−180 copyright 1984 and H. Okamoto, Journal of Phase Equilibria (and Diffusion) Vol. 31, Issue 6, pp. 580−581 copyright 2010, respectively).

can be seen that on many of 4-anion unit cells near the surface in the $1T'$-$ReSe_2$ only two or three of the anions are bright enough to be Re atoms (highlighted by orange arrows), indicating that Mo atoms have replaced them in the $1T'$ lattice. However, the interface between the two phases is atomically sharp, and moreover, extends as an atomically sharp region across large sections of the monolayer region. The area in the dashed box in Figure 2b is shown in Figure 2c, and the positions of all the atoms in the 2H phase and all the anions in the $1T'$ phase results are established and shown in Figure 2d.

The interface is unstable under the intense electron irradiation of the beam, as a result high-quality magnification images of the interface are difficult to achieve. This phenomenon is demonstrated directly in Figure S6, where the same interface can be seen to degrade from the zigzag interface shown in Figure 2b−d, to an amorphous configuration in sequential images. This amorphization is also likely to be responsible for the high-contrast regions at the top of the image in Figure 2a.

Due to this instability, HAADF images are all acquired with short pixel dwell times and low pixel densities to minimize any perturbations to the crystal structure, and as a result many of the cation sites with smaller lattice spacings in the 2D projection cannot be resolved from one another. Rather than show some of the $1T'$ cation sites and not others, we have chosen to define the $1T'$ crystal just by the easily resolved anion sites. The fractional HAADF intensities of all the labeled sites are shown in Figure 2e and show that red-sites are the Mo and the yellow sites are the Se_2 columns (due to the higher

HAADF intensities); thus, we can look back on the atom labeled image in Figure 2d and see that the atomically sharp interface takes place on the zigzag plane and is Se terminated. Regardless of the instability under, the zigzag termination is readily and consistently observed throughout the sample, moreover it is always observed to be atomically sharp (Figure S7).

Figure 3a shows the atomic arrangements in potential two interfacial structures along the low-energy zigzag direction, α and β, between monolayers of 1H $MoSe_2$ and $1T'$ $ReSe_2$. The α-interface is characterized by the presence of 3-fold-coordinated Se anions at the $MoSe_2$/$ReSe_2$ interface, whereas the β-interface contains only 4-fold coordinated Se ions at the interface following the terminology used by Lin et al. for interfaces between 2H and 1T phases of MoS_2.[35] A comparison of the simulated interfacial structures with high-resolution TEM micrographs of the interface shows good correspondence between predicted and observed atomic positions for the α interface (Figure 3b). This observation is also supported by DFT-computed interfacial energies for the α- and β-interfaces, which shows that the nonmagnetic α-interface represents the lowest energy configuration with an interfacial energy of 0.24 eV/Å, compared to 0.34 eV/Å (Figure S8 in the Supporting Information).

To understand the composition of $MoSe_2$ and $ReSe_2$ crystals that constitute the experimental heterostructure and to quantify the extent of mutual doping, we calculate the free energy of alloyed $Mo_{1-x}Re_xSe_2$ monolayer crystals in the H and T' crystal structures from the DFT energies of formation
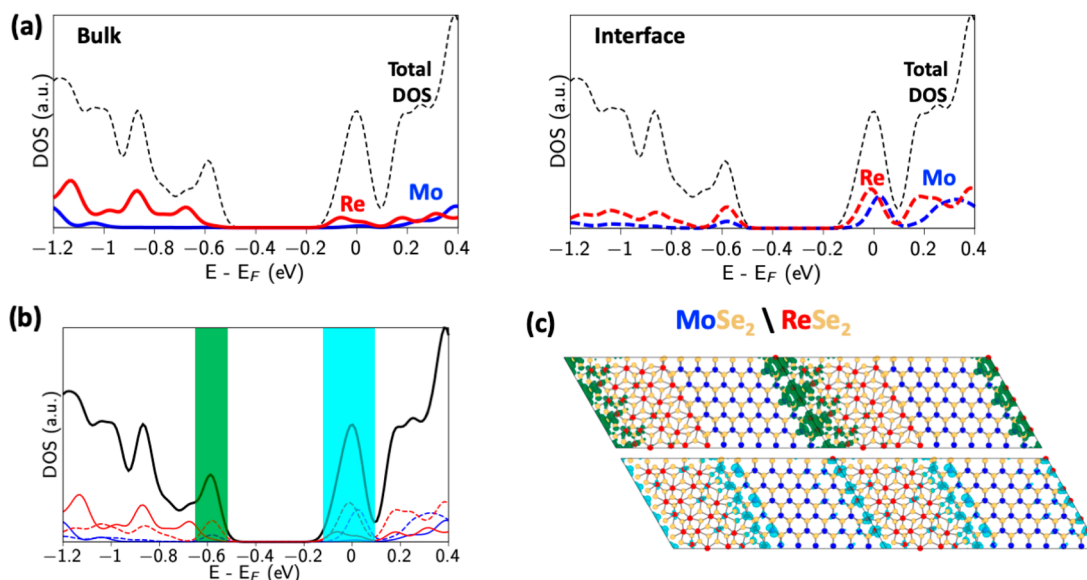
Figure 5. Electronic structure of lateral heterostructures. (a) Partial density of electronic states in the RMS heterostructure supercell, showing contributions from bulk-like (solid) and interfacial (dashed) atoms. It can be seen that interfacial Mo and Re atoms contribute significantly to the band edge states in both the valence and conduction bands, whereas the contribution from bulklike atoms, particularly Mo, is negligible. (b,c) Isosurfaces of the spatial distribution of valence and conduction band edge states show that these band gap reducing states are localized within one lattice constant from the $MoSe_2/ReSe_2$ interface.

and the analytical free energy of mixing (of Mo and Re ions) in the cation sublattice. The common tangent to these two free energy curves identifies the composition of H-phase $Mo_{1-\delta}Re_\delta Se_2$ and T′-phase $Re_{1-\delta}Mo_\delta Se_2$ ($\delta \ll 1$) crystals that are in chemical equilibrium across the interface in a lateral heterostructure. Figure 3c,d shows that the lateral heterostructure is formed between a 2H $MoSe_2$ crystal containing 0.43% Re doping and a 1T′ $ReSe_2$ crystal Mo substitutional defects in 1.73% of all cation sites, consistent with the experimentally observed marginal doping of Re atoms in $MoSe_2$ and vice versa (Figure 2).

The two-dimensional $Re_{1-x}Mo_xSe_2$ system can also be understood via metallurgical phase diagrams previously established in the literature. In order to understand the special nature of this system, we first consider the commonly studied 2D $W_{1-x}Mo_xX_2$ system (X = chalcogen). Figure 4a shows the binary Mo−W phase diagram. Molybdenum and tungsten are isomorphous and hence show complete miscibility at all compositions. Hence the phase diagram has (only) three principal regions—solid solution, mixed solid solution + liquid, and complete liquid at higher temperatures. Therefore, the mixed alloy phase is thermodynamically preferred for this system at all compositions. Such transition metal atom substitution/mixing in 2D TMDCs can be understood as every monolayer consists of three sublayers: a transition metal atom layer sandwiched between two chalcogen atom layers.

Therefore, if the experiment consists of synthesizing 2D TMDC alloys, the mixing occurs only in the middle sublayer with the top and bottom chalcogen atom layers remaining intact. As a result, synthesizing 2D MoX_2−WX_2 heterostructures via CVD involves kinetic considerations such as changing the type and nature of the Mo and W precursors and growth temperatures to introduce substantial difference in evaporation times and rates so as to prefer the growth of one type of phase (MoX_2) before the other (WX_2). Another example is in the analysis of the 1D heterojunction between 2D $MoSe_2$ and WSe_2 heterostructures via atomically resolved

HAADF-STEM imaging as reported by Huang et al.[28] They observe that the heterojunction shows a strong gradient of W atoms from the WSe_2 domain into the $MoSe_2$ one and vice versa. This phenomenon directly arises out of the isomorphous and miscible nature of molybdenum and tungsten.

On the other hand, the molybdenum−rhenium system is completely different. Figure 4b shows the binary Mo−Re phase diagram. In stark contrast to the simplicity of the Mo−W system, the Mo−Re system shows rich phase mixing and segregation behavior as a function of temperature and composition. For instance, rhenium is (partly) miscible in molybdenum up to a maximum concentration Re ∼ 40%. We have demonstrated this in our previous work on synthesizing 2D $Re_{1-x}Mo_xSe_2$ alloys with tunable composition via CVD.[32] At greater Re compositions, the binary system shows completely different structural phase(s) as shown in the figure. As we change fraction of Mo precursor over the Re one (in this work) while keeping the rest of the growth parameters essentially unchanged, we find that the 2D $Re_{1-x}Mo_xSe_2$ system forms after which the molybdenum precipitates out of the solid solution to form distinct $MoSe_2$ domains inside of the $ReSe_2$-rich matrix, all at the monolayer level. This can be easily seen via Raman spectroscopy and is further evidence for the evolution of the distinct $MoSe_2$ and $ReSe_2$ 2D domains. Figure 4c shows the optical images of five 2D $Re_{1-x}Mo_xSe_2$ samples; from left to right, the first three showing mixed nature and the other two showing optically visible segregation. Figure 4d shows the corresponding Raman spectra of these five samples (from spots marked on the images in Figure 4c). The strong A_{1g} mode from 2H $MoSe_2$ at ∼240 cm^{-1} in Sample I decreases in intensity with increasing Re concentration in Sample II, and finally disappearing entirely for Sample III with emergence of new modes reminiscent of $ReSe_2$ phase. Sample IV shows a clear heterostructure of triangular $MoSe_2$ domains dispersed in a matrix composed of Sample III-type composition as shown from the distinct Raman spectra. This may be an example of partial segregation as well as the sizes of

individual domains not thermodynamically large enough for the diffraction limited Raman probe to distinguish. For Sample V, the distinction is much stronger as the Raman spectra of the darker and lighter regions show complete phase segregation of $MoSe_2$ from $ReSe_2$ indicative of larger domain sizes as understood from the phase diagram. The dissimilarity between Mo and Re is also seen in the atomically resolved HAADF-STEM image in Figure 2c with the sharp 1D junction between the $MoSe_2$ and $ReSe_2$ monolayers unlike the diffusion of Mo and W into each other as reported for monolayer $MoSe_2-WSe_2$ heterostructures.

The formation of a lateral heterostructure between semiconducting monolayer $MoSe_2$ and monolayer $ReSe_2$ closes the band gap in the supercell containing the heterostructure interface. This reduction in band gap down from a value of 1.4 eV in monolayer $MoSe_2$ occurs via the formation of band-edge states at the valence and conduction edges. Figure 5a shows the partial density of electronic states in the $MoSe_2/ReSe_2$ heterostructure showing the contribution of interfacial Mo and Re atoms as well as "bulklike" atoms far away from the interface. Figure 5a shows that both valence and conduction band edge states arise from interfacial Mo and Re atoms with bulklike atoms contributing only negligibly to density of states in the range of $(-0.6, 0.1)$ eV around the Fermi level. Figure 5b,c depict the isosurface of the valence and conduction band-edge charge densities, showing spatial localization of these band gap reducing states to within on lattice constant of the interface with little contribution from bulk-like atoms in the $MoSe_2$ or $ReSe_2$ monolayers. This small band gap in the type-I electronic heterojunction between $2H\text{-}MoSe_2$ and $1T'\text{-}ReSe_2$ results in rectifying behavior at the lateral interface, which is evident in electrical characterization of the synthesized heterostructure device (Figures S9 and S10 of the Supporting Information).

In conclusion, we demonstrate the chemical vapor deposition synthesis of monolayer $2H$ $MoSe_2-1T'$ $ReSe_2$ lateral heterostructures on single crystal sapphire substrates containing a smooth, atomically sharp interface along the zigzag directions between the parent phases as verified via high-resolution HAADF-STEM imaging. Raman and XPS spectra show that the interface formed between the two nominally pure phases with negligible interdiffusion of rhenium and molybdenum atoms. We also utilize the phase diagrams of the binary Mo−Re system to differentiate it from commonly reported Mo−W chalcogenide systems toward its unique thermodynamically dictated preference for alloy versus heterostructure formation at the monolayer limit. This is supported by calculations of free energies and interfacial energies using density functional theory, which also demonstrates how Mo and Re band edge states lead to strong reduction in electronic band gaps of the heterostructures. This work illustrates the use of atomic heterojunctions between two structurally and chemically distinct 2D materials as a potential method for tailoring the electronic structure for optoelectronic applications.

■ ASSOCIATED CONTENT

Ⓢ Supporting Information

The Supporting Information is available free of charge on the ACS Publications website at DOI: 10.1021/acs.nano-lett.9b02476.

PL spectra, AFM images and analysis, additional HAADF-STEM images, device performance (PDF)

■ AUTHOR INFORMATION

Corresponding Authors
*E-mail: priyav@usc.edu.
*E-mail: cst311@gmail.com.
*E-mail: ajayan@rice.edu.

ORCID Ⓘ
Aravind Krishnamoorthy: 0000-0001-6778-2471
Jordan A. Hachtel: 0000-0002-9728-0920
Sandhya Susarla: 0000-0003-1773-0993
Jongwon Yoon: 0000-0001-6425-6046
Palash Bharadwaj: 0000-0003-0722-6697
James M. Tour: 0000-0002-8479-9328
Aiichiro Nakano: 0000-0003-3228-3896
Priya Vashishta: 0000-0003-4683-429X
Chandra Sekhar Tiwary: 0000-0001-9760-9768

Present Address
#(C.S.T.) Metallurgical and Materials Engineering, Indian Institute of Technology, Kharagpur, West Bengal, India.

Author Contributions
A.A. synthesized the samples and performed the Raman/PL measurements and device fabrication. S.S. performed XPS measurements. J.A.H. and J.C.I. performed STEM imaging and analysis. L.M.S. and P.B. helped with AFM measurements. J.Y. and J.M.T. performed electrical measurements. A.K., A.N., R.K.K., and P.D.V. performed DFT simulations. P.V., C.S.T., and P.M.A. advised the research. The manuscript was written through contributions of all authors. All authors have given approval to the final version of the manuscript.

Notes
The authors declare no competing financial interest.

■ REFERENCES

(1) Manzeli, S.; Ovchinnikov, D.; Pasquier, D.; Yazyev, O. V.; Kis, A. 2D Transition Metal Dichalcogenides. *Nat. Rev. Mater.* **2017**, *2*, 17033.

(2) Wang, Q. H.; Kalantar-Zadeh, K.; Kis, A.; Coleman, J. N.; Strano, M. S. Electronics and Optoelectronics of Two-Dimensional Transition Metal Dichalcogenides. *Nat. Nanotechnol.* **2012**, *7*, 699−712.

(3) Ugeda, M. M.; Bradley, A. J.; Shi, S.-F.; da Jornada, F. H.; Zhang, Y.; Qiu, D. Y.; Ruan, W.; Mo, S.-K.; Hussain, Z.; Shen, Z.-X.; et al. *Nat. Mater.* **2014**, *13*, 1091.

(4) Geim, A. K.; Novoselov, K. S. The Rise of Graphene. *Nat. Mater.* **2007**, *6*, 183−191.

(5) Wang, X.; Gong, Y.; Shi, G.; Chow, W. L.; Keyshar, K.; Ye, G.; Vajtai, R.; Lou, J.; Liu, Z.; Ringe, E.; et al. *ACS Nano* **2014**, *8*, 5125−5131.

(6) Mann, J.; Ma, Q.; Odenthal, P. M.; Isarraraz, M.; Le, D.; Preciado, E.; Barroso, D.; Yamaguchi, K.; von Son Palacio, G.; Nguyen, A.; et al. *Adv. Mater.* **2014**, *26*, 1399−1404.

(7) Alem, N.; Erni, R.; Kisielowski, C.; Rossell, M. D.; Gannett, W.; Zettl, A. Atomically Thin Hexagonal Boron Nitride Probed by Ultrahigh-Resolution Transmission Electron Microscopy. *Phys. Rev. B: Condens. Matter Mater. Phys.* **2009**, *80*, 155425.

(8) Song, J.-G.; Ryu, G. H.; Lee, S. J.; Sim, S.; Lee, C. W.; Choi, T.; Jung, H.; Kim, Y.; Lee, Z.; Myoung, J.-M.; et al. *Nat. Commun.* **2015**, *6*, 7817.

(9) Keyshar, K.; Gong, Y.; Ye, G.; Brunetto, G.; Zhou, W.; Cole, D. P.; Hackenberg, K.; He, Y.; Machado, L.; Kabbani, M.; et al. *Adv. Mater.* **2015**, *27*, 4640−4648.

(10) Geim, A. K.; Grigorieva, I. V. Van Der Waals Heterostructures. *Nature* **2013**, *499*, 419−425.

(11) Lin, M.; Wu, D.; Zhou, Y.; Huang, W.; Jiang, W.; Zheng, W.; Zhao, S.; Jin, C.; Guo, Y.; Peng, H.; et al. *J. Am. Chem. Soc.* **2013**, *135*, 13274−13277.

(12) Gong, Y.; Lin, J.; Wang, X.; Shi, G.; Lei, S.; Lin, Z.; Zou, X.; Ye, G.; Vajtai, R.; Yakobson, B. I.; et al. *Nat. Mater.* **2014**, *13*, 1135−1142.

(13) Huang, X.; Zeng, Z.; Bao, S.; Wang, M.; Qi, X.; Fan, Z.; Zhang, H. Solution-Phase Epitaxial Growth of Noble Metal Nanostructures on Dispersible Single-Layer Molybdenum Disulfide Nanosheets. *Nat. Commun.* **2013**, *4*, 1444.

(14) Chen, W.; Yang, Y.; Zhang, Z.; Kaxiras, E. Properties of In-Plane Graphene/MoS 2 Heterojunctions. *2D. 2D Mater.* **2017**, *4*, 045001.

(15) Lin, Y.-C.; Lu, N.; Perea-Lopez, N.; Li, J.; Lin, Z.; Peng, X.; Lee, C. H.; Sun, C.; Calderin, L.; Browning, P. N.; et al. *ACS Nano* **2014**, *8*, 3715−3723.

(16) Yu, H.; Kutana, A.; Yakobson, B. I. Carrier Delocalization in Two-Dimensional Coplanar p−n Junctions of Graphene and Metal Dichalcogenides. *Nano Lett.* **2016**, *16*, 5032−5036.

(17) Lee, C.-H.; Lee, G.-H.; van der Zande, A. M.; Chen, W.; Li, Y.; Han, M.; Cui, X.; Arefe, G.; Nuckolls, C.; Heinz, T. F.; et al. *Nat. Nanotechnol.* **2014**, *9*, 676.

(18) Liu, Y.; Weiss, N. O.; Duan, X.; Cheng, H.-C.; Huang, Y.; Duan, X. Van Der Waals Heterostructures and Devices. *Nat. Rev. Mater.* **2016**, *1*, 16042.

(19) Lei, Y.; Pakhira, S.; Fujisawa, K.; Wang, X.; Iyiola, O. O.; Perea López, N.; Laura Elías, A.; Pulickal Rajukumar, L.; Zhou, C.; Kabius, B.; et al. *ACS Nano* **2017**, *11*, 5103−5112.

(20) Duan, X.; Wang, C.; Shaw, J. C.; Cheng, R.; Chen, Y.; Li, H.; Wu, X.; Tang, Y.; Zhang, Q.; Pan, A.; et al. *Nat. Nanotechnol.* **2014**, *9*, 1024−1030.

(21) Bogaert, K.; Liu, S.; Chesin, J.; Titow, D.; Gradečak, S.; Garaj, S. Diffusion-Mediated Synthesis of MoS2/WS2 Lateral Heterostructures. *Nano Lett.* **2016**, *16*, 5129−5134.

(22) Ullah, F.; Sim, Y.; Le, C. T.; Seong, M.-J.; Jang, J. I.; Rhim, S. H.; Tran Khac, B. C.; Chung, K.-H.; Park, K.; Lee, Y.; et al. *ACS Nano* **2017**, *11*, 8822−8829.

(23) Gong, Y.; Lei, S.; Ye, G.; Li, B.; He, Y.; Keyshar, K.; Zhang, X.; Wang, Q.; Lou, J.; Liu, Z.; et al. *Nano Lett.* **2015**, *15*, 6135−6141.

(24) Hong, X.; Kim, J.; Shi, S.-F.; Zhang, Y.; Jin, C.; Sun, Y.; Tongay, S.; Wu, J.; Zhang, Y.; Wang, F. Ultrafast Charge Transfer in Atomically Thin MoS2/WS2 Heterostructures. *Nat. Nanotechnol.* **2014**, *9*, 682.

(25) Hill, H. M.; Rigosi, A. F.; Rim, K. T.; Flynn, G. W.; Heinz, T. F. Band Alignment in MoS2/WS2 Transition Metal Dichalcogenide Heterostructures Probed by Scanning Tunneling Microscopy and Spectroscopy. *Nano Lett.* **2016**, *16*, 4831−4837.

(26) Chen, K.; Wan, X.; Wen, J.; Xie, W.; Kang, Z.; Zeng, X.; Chen, H.; Xu, J.-B. Electronic Properties of MoS2−WS2 Heterostructures Synthesized with Two-Step Lateral Epitaxial Strategy. *ACS Nano* **2015**, *9*, 9868−9876.

(27) He, X.; Li, H.; Zhu, Z.; Dai, Z.; Yang, Y.; Yang, P.; Zhang, Q.; Li, P.; Schwingenschlogl, U.; Zhang, X. Strain Engineering in Monolayer WS2, MoS2, and the WS2/MoS2 Heterostructure. *Appl. Phys. Lett.* **2016**, *109*, 173105.

(28) Huang, C.; Wu, S.; Sanchez, A. M.; Peters, J. J. P.; Beanland, R.; Ross, J. S.; Rivera, P.; Yao, W.; Cobden, D. H.; Xu, X. Lateral Heterojunctions within Monolayer MoSe2−WSe2 Semiconductors. *Nat. Mater.* **2014**, *13*, 1096−1101.

(29) Susarla, S.; Hachtel, J. A.; Yang, X.; Kutana, A.; Apte, A.; Jin, Z.; Vajtai, R.; Idrobo, J. C.; Lou, J.; Yakobson, B. I.; et al. *Adv. Mater.* **2018**, *30*, 1804218.

(30) Jariwala, B.; Voiry, D.; Jindal, A.; Chalke, B. A.; Bapat, R.; Thamizhavel, A.; Chhowalla, M.; Deshmukh, M.; Bhattacharya, A. Synthesis and Characterization of ReS2 and ReSe2 Layered Chalcogenide Single Crystals. *Chem. Mater.* **2016**, *28*, 3352−3359.

(31) Yang, S.; Tongay, S.; Li, Y.; Yue, Q.; Xia, J.-B.; Li, S.-S.; Li, J.; Wei, S.-H. Layer-Dependent Electrical and Optoelectronic Responses of ReSe2 Nanosheet Transistors. *Nanoscale* **2014**, *6*, 7226−7231.

(32) Kochat, V.; Apte, A.; Hachtel, J. A.; Kumazoe, H.; Krishnamoorthy, A.; Susarla, S.; Idrobo, J. C.; Shimojo, F.; Vashishta, P.; Kalia, R.; et al. *Adv. Mater.* **2017**, *29*, 1703754.

(33) Wolverson, D.; Crampin, S.; Kazemi, A. S.; Ilie, A.; Bending, S. J. Raman Spectra of Monolayer, Few-Layer, and Bulk ReSe2: An Anisotropic Layered Semiconductor. *ACS Nano* **2014**, *8*, 11154−11164.

(34) Ryder, C. R.; Wood, J. D.; Wells, S. A.; Hersam, M. C. Chemically Tailoring Semiconducting Two-Dimensional Transition Metal Dichalcogenides and Black Phosphorus. *ACS Nano* **2016**, *10*, 3900−3917.

(35) Lin, Y. C.; Dumcencon, D. O.; Huang, Y. S.; Suenaga, K. Atomic Mechanism of the Semiconducting-to-Metallic Phase Transition in Single-Layered MoS2. *Nat. Nanotechnol.* **2014**, *9*, 391−396.